*J. Fluid Mech.* (1969), *vol.* 36, *part* 1, *pp.* 33–54
*Printed in Great Britain*



# Numerical study of natural convection in an enclosure with localized heating from below—creeping flow to the onset of laminar instability

By K. E. TORRANCE AND J. A. ROCKETT
National Bureau of Standards, Washington, D.C., 20234

(Received 24 June 1968)

An analytical study was made of the natural convection induced in an enclosure by a small hot spot centrally located on the floor. The enclosure was a circular cylinder, vertically oriented, with height equal to radius. A Prandtl number of 0·7 (air) was assumed; the Grashof number ($Gr$) was based on cylinder height and hot spot temperature. The equations of fluid flow in axisymmetric cylindrical co-ordinates were simplified with the Boussinesq approximation. The equations were solved numerically with a computationally stable, explicit method. The computation, starting from quiescent conditions, proceeded through the initial transient to the fully developed flow. Solutions were obtained for $Gr$ from $4 \times 10^4$ to $4 \times 10^{10}$. The theoretical flows are in excellent agreement with experimentally observed laminar flows ($Gr \lesssim 1{\cdot}2 \times 10^9$) which are discussed in a companion paper, Torrance, Orloff & Rockett (1969). Turbulence was observed experimentally for $Gr \gtrsim 1{\cdot}2 \times 10^9$. When the theoretical calculations were extended to $Gr = 4 \times 10^{10}$, a periodic vortex shedding developed, suggestive of the onset of laminar instability. The theoretical results reveal a $\sqrt{Gr}$ scaling for the initial flow transients and, at large $Gr$, the velocities and heat transfer rates.

## 1. Introduction

Thermally induced fluid motion in confined spaces is of widespread interest in fluid mechanics. Indeed, numerous examples of such flows may readily be cited from everyday experience. The present study was motivated by a hopefully not-so-everyday experience; namely, the transient natural convection arising from an incipient fire in a room. Most fire detectors depend upon this natural convection to carry sensible evidence of the fire to a detector. A knowledge of the induced convective flow is thus essential for the design of an efficient fire detection and localization system. A full understanding of these flows represents a formidable task, inasmuch as they depend upon the size and location of the fire, the room geometry, and a host of other variables. This work was restricted to that portion of the general problem in which laminar flows prevail and to one simple geometry.

Transient and steady-state convective flows are considered in a vertical circular cylinder with the fire simulated by a small heat source in the centre of the floor. Two-dimensional, axisymmetric cylindrical co-ordinates are employed, thereby

precluding the possibility of computing completely turbulent flows. The governing non-linear partial differential equations for energy and vorticity are approximated by an explicit finite difference scheme. The scheme differs from the numerical methods of Barakat & Clark (1966) and Wilkes & Churchill (1966) in that vorticity and energy are conserved within the finite difference mesh. This is essential for a faithful approximation of the physical system. A special formulation is used for the non-linear derivatives which leads to unconditional numerical stability. The numerical methods of Fromm (1964, chapter 10) and Wilkes & Churchill (1966) use higher order approximations for these non-linear derivatives, but do not possess the stability of the present method. This stability permits us to study flows where the non-linear convective terms can be dominant, as in the present problem.

A formal statement of the problem is presented in § 2, followed by a description of the numerical method in 3 and results in 4.

## 2. Formulation of the problem

Consider the motion of a viscous fluid within a vertical cylinder of height $a$ and radius $b$ (see figure 1). Erect a co-ordinate system $(x, r)$ in the centre of the base. The fluid is initially motionless and at a uniform temperature $T_0$. The enclosure walls are also at this temperature, except for a small centrally located circular spot on the base of radius $c$ which is at a temperature $T_h > T_0$. The problem is to find the subsequent velocities, temperatures, and rates of heat transfer to the enclosure as functions of time and position; and to obtain the fully developed solution.

The Boussinesq approximation is used; in this density ($\rho$) is assumed constant except for the generation of buoyancy forces. Other fluid properties are taken as constant: kinematic viscosity ($\nu$), thermal diffusivity ($\kappa$) and volume expansion coefficient ($\beta$). We introduce the following dimensionless quantities: time, $\tau = (\kappa/a^2)t$; vertical and radial co-ordinates, $X = x/a$ and $R = r/a$; vertical and radial components of velocity, $U = (a/\kappa)u$ and $V = (a/\kappa)v$; and temperature $\theta = (T - T_0)/(T_h - T_0)$.

The flow is assumed to be axisymmetric. Therefore, the continuity equation is automatically satisfied by the introduction of a dimensionless stream function $\Psi$. Furthermore, the dimensionless vorticity vector defined by $\boldsymbol{\Omega} = \text{curl } \mathbf{U}$ has only an azimuthal component, $\boldsymbol{\Omega} = \Omega\mathbf{k}$, where $\mathbf{k}$ is the azimuthal unit vector and $\Omega = \partial V/\partial X - \partial U/\partial R$. The following relations are provided by the definitions of stream function and vorticity

$$U = \frac{1}{R}\frac{\partial \Psi}{\partial R}, \quad V = -\frac{1}{R}\frac{\partial \Psi}{\partial X} \tag{1}$$

and

$$\frac{1}{R}\frac{\partial^2 \Psi}{\partial X^2} + \frac{\partial}{\partial R}\left(\frac{1}{R}\frac{\partial \Psi}{\partial R}\right) = -\Omega. \tag{2}$$

The energy equation takes the form

$$\frac{\partial \theta}{\partial \tau} + \frac{\partial (U\theta)}{\partial X} + \frac{1}{R}\frac{\partial (RV\theta)}{\partial R} = \frac{\partial^2 \theta}{\partial X^2} + \frac{1}{R}\frac{\partial}{\partial R}\left(R\frac{\partial \theta}{\partial R}\right) \tag{3}$$

in the absence of viscous dissipation and compressibility effects. The equation of continuity was not used to rearrange the transport terms on the left-hand side.

By taking the curl of the momentum equations pressure is eliminated and we obtain the equation for vorticity.†

$$\frac{\partial\Omega}{\partial\tau}+\frac{\partial(U\Omega)}{\partial X}+\frac{\partial(V\Omega)}{\partial R}=-GrPr^2\frac{\partial\theta}{\partial R}+Pr\left[\frac{\partial^2\Omega}{\partial X^2}+\frac{\partial}{\partial R}\left(\frac{1}{R}\frac{\partial(R\Omega)}{\partial R}\right)\right]. \tag{4}$$

This equation contains the Grashof number $Gr = g\beta(T_h - T_0)a^3/\nu^2$ and the Prandtl number $Pr = \nu/\kappa$. The acceleration of gravity is denoted by $g$.

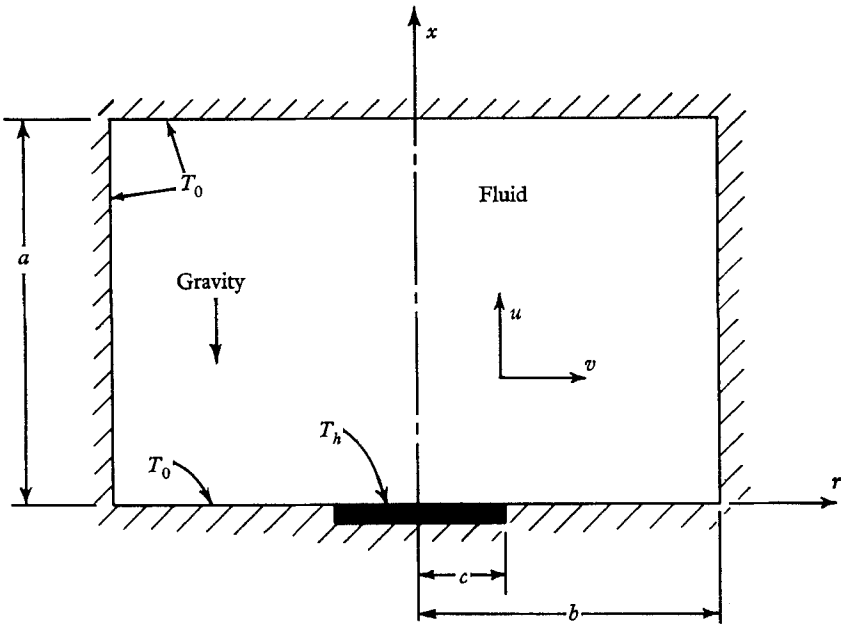


FIGURE 1. Cylindrical enclosure and co-ordinate system.

Equations (1)–(4) are subject to specific initial conditions and boundary conditions. The initial conditions are:

$$\tau < 0, \quad 0 \leqslant X \leqslant 1, \quad 0 \leqslant R \leqslant R_b; \quad \Omega = \theta = 0. \tag{5}$$

The boundary conditions‡ for $\tau \geqslant 0$ are:

$$\left.\begin{array}{lll} X = 0, & 0 \leqslant R \leqslant R_b; & \Psi = \partial\Psi/\partial X = 0. \\ & 0 \leqslant R < R_c; & \theta = 1. \\ & R = R_c; & \theta = 0{\cdot}5. \\ & R_c < R \leqslant R_b; & \theta = 0. \\ X = 1, & \text{all } R; & \Psi = \partial\Psi/\partial X = \theta = 0. \\ R = 0, & \text{all } X; & \Psi = \Omega = \partial\theta/\partial R = 0. \\ R = R_b, & \text{all } X; & \Psi = \partial\Psi/\partial R = \theta = 0. \end{array}\right\} \tag{6}$$

† Equation (4) is equivalent to equation (19·11–1) of Milne-Thomson (1960) if the buoyancy source term $Gr\,Pr^2\partial\theta/\partial R$ is added.

‡ Note that explicit boundary conditions for vorticity on the solid boundaries are not available. Fortunately, this causes no difficulty with the solution method used, as will be explained later.

The boundary conditions introduce two parameters: the aspect ratio of the enclosure (radius/height) $R_b = b/a$ and the relative size of the heat source (heat source radius/enclosure height) $R_c = c/a$.

The velocities $U$ and $V$ are retained explicitly in the problem formulation, because their computed values yield an immediate picture of the flow pattern. However, an examination of (1)–(6) reveals that the essential dependent variables are $\theta$, $\Omega$, and $\Psi$, while the independent variables are $X$, $R$ and $\tau$. The parameters of the problem are $Gr$, $Pr$, $R_b$ and $R_c$.

## 3. Numerical method

### 3.1. *The grid system*

Equations (1)–(4) will be called the velocity, stream function, temperature and vorticity equations, respectively. The temperature and vorticity equations are parabolic, while the stream function equation is elliptic. An approximation to their solution will be obtained at a finite number of grid points having co-ordinates $X = i\Delta X$, $R = j\Delta R$, and at discrete times $\tau_n$ where $i$ , $j$ and $n$ are integers. The grid spacings in the $X$ and $R$ directions are denoted by $\Delta X$ and $\Delta R$. The symbol $\tau_n$ denotes the time level after the $n$th time step $\Delta\tau_n$; $\tau_n = \tau_{n-1} + \Delta\tau_n$. The size of $\Delta\tau$ is limited by stability considerations, and is calculated before each time advancement.

The values of $\theta$, $\Omega$, $\Psi$, $U$ and $V$ at each grid point should be thought of as average values over a small volume of fluid surrounding the point. This is the lumped mass concept, in which the physical system shown in figure 1 is replaced by a system of interconnected nodes. Except along the centreline, each interior node replaces a ring of fluid of height $\Delta X$ and radial thickness $\Delta R$. The exchange of mass, energy and vorticity via the interconnexions between the nodes can then be associated with the various terms arising from the finite difference approximation.

### 3.2. *The finite difference scheme*

Suppose that all quantities are known at a time $\tau$ (the initial condition corresponds to the special case $\tau = 0$). The fields of temperature and vorticity at interior grid points are advanced across a time step $\Delta\tau$ to the new level $\tau + \Delta\tau$ by using explicit finite difference approximations to the temperature and vorticity equations. At any grid point the term $\partial\theta/\partial R$ in the vorticity equation and the velocities $U$ and $V$ are treated as constants over the time step. All linear space derivatives are approximated by three-point central differences.

To preserve the stability of the numerical scheme the non-linear space derivatives ($\partial(U\theta)/\partial X, \partial(RV\theta)/\partial R, \partial(U\Omega)/\partial X$ and $\partial(V\Omega)/\partial R$) are approximated with special three point non-central differences. The special forms are

$$\left(\frac{\partial(Uf)}{\partial X}\right)_{i,j} = \frac{1}{\Delta X}\left(\frac{U_{i+1,j}+U_{i,j}}{2} f_{i,j} - \frac{U_{i,j}+U_{i-1,j}}{2} f_{i-1,j}\right) \tag{7a}$$

when the coefficients $\frac{1}{2}(U_{i+1,j}+U_{i,j})$ and $\frac{1}{2}(U_{i,j}+U_{i-1,j})$ are positive and

$$\left(\frac{\partial(Uf)}{\partial X}\right)_{i,j} = \frac{1}{\Delta X}\left(\frac{U_{i+1,j}+U_{i,j}}{2} f_{i+1,j} - \frac{U_{i,j}+U_{i-1,j}}{2} f_{i,j}\right) \tag{7b}$$

when the coefficients are negative. The variable $f$ represents either $\theta$ or $\Omega$ and the subscripts denote the spatial location of grid points. When the mean velocities $\frac{1}{2}(U_{i+1,j}+U_{i,j})$ and $\frac{1}{2}(U_{i,j}+U_{i-1,j})$ are of different sign, a mixed expression is required which contains one term from each of equations (7), as appropriate. A similar procedure is used to approximate $\partial(RV\theta)/\partial R$ and $\partial(V\Omega)/\partial R$ according to the sign of $\frac{1}{2}(V_{i,j+1}+V_{i,j})$ and $\frac{1}{2}(V_{i,j}+V_{i,j-1})$.

When the mean velocity $\frac{1}{2}(U_{i+1,j}+U_{i,j})$, for example, is multiplied by $f_{i,j}$ or $f_{i+1,j}$ in equations (7), the product represents a convective transport of $f$ between node points $(i+1,j)$ and $(i,j)$. The selection of $f_{i,j}$ or $f_{i+1,j}$, according to the sign of the mean velocity, is necessary for $f$ to be strictly conserved in transport between the nodes. A Taylor series analysis of this scheme reveals that one of the truncation errors introduces a false viscosity and heat diffusivity into the numerical solutions of the vorticity and temperature equations. This error is significant only at high Grashof numbers, where the false viscosity enhances fluid stability. The error can be largely eliminated by using the more conventional three point central differences, but this scheme leads to major problems of numerical stability. Stability can be achieved at high Grashof numbers only by using a very fine mesh, which leads to prohibitively large computer storage requirements. For additional details see Torrance (1968), wherein comparisons of the stability, traucation errors, and conservation properties of several numerical schemes are provided.

The relevant finite difference approximations to the temperature and vorticity equations are (8) and (9) for the case where the non-linear derivatives are represented by forms similar to (7*a*). The equations are used to advance across the time step $\Delta\tau$ from time $\tau$ to time $\tau'=\tau+\Delta\tau$. Primed and unprimed variables respectively denote values at time levels $\tau'$ and $\tau$. Temperature is advanced first with

$$\frac{\theta'_{i,j}-\theta_{i,j}}{\Delta\tau}+\frac{(U_{i+1,j}+U_{i,j})\theta_{i,j}-(U_{i,j}+U_{i-1,j})\theta_{i-1,j}}{2\Delta X}$$
$$+\frac{(j+1/2)(V_{i,j+1}+V_{i,j})\theta_{i,j}-(j-1/2)(V_{i,j}+V_{i,j-1})\theta_{i,j-1}}{2j\Delta R}$$
$$=\frac{\theta_{i+1,j}-2\theta_{i,j}+\theta_{i-1,j}}{(\Delta X)^2}+\frac{(j+1/2)\theta_{i,j+1}-2j\theta_{i,j}+(j-1/2)\theta_{i,j-1}}{j(\Delta R)^2} \tag{8}$$

followed by

$$\frac{\Omega'_{i,j}-\Omega_{i,j}}{\Delta\tau}+\frac{(U_{i+1,j}+U_{i,j})\Omega_{i,j}-(U_{i,j}+U_{i-1,j})\Omega_{i-1,j}}{2\Delta X}$$
$$+\frac{(V_{i,j+1}+V_{i,j})\Omega_{i,j}-(V_{i,j}+V_{i,j-1})\Omega_{i,j-1}}{2\Delta R}=-Gr\,Pr^2\frac{\theta'_{i,j+1}-\theta'_{i,j-1}}{2\Delta R}$$
$$+Pr\left\{\frac{\Omega_{i+1,j}-2\Omega_{i,j}+\Omega_{i-1,j}}{(\Delta X)^2}\right.$$
$$\left.+\frac{[(j+1)/(j+1/2)]\Omega_{i,j+1}-[(j/(j+1/2)+j/(j-1/2)]\Omega_{i,j}+[(j-1)/(j-1/2)]\Omega_{i,j-1}}{(\Delta R)^2}\right\}. \tag{9}$$

Note that the derivatives containing the radial co-ordinate $R$ introduce this co-ordinate at integer and half-integer $j$-values, as appropriate. At the centreline, a special form of (8) is used which incorporates boundary conditions (6) at $R = 0$:

$$\frac{\theta'_{i,0}-\theta_{i,0}}{\Delta\tau}+\frac{(U_{i+1,0}+U_{i,0})\theta_{i,0}-(U_{i,0}+U_{i-1,0})\theta_{i-1,0}}{2\Delta X}+\frac{2V_{i,1}}{\Delta R}\theta_{i,0}=\frac{\theta_{i+1,0}-2\theta_{i,0}+\theta_{i-1,0}}{(\Delta X)^2}+\frac{4(\theta_{i,1}-\theta_{i,0})}{(\Delta R)^2}. \tag{10}$$

Equations (8), (9) and (10) thus permit $\theta'_{i,j}$ and $\Omega'_{i,j}$ at all interior grid points to be explicitly calculated in terms of known quantities.

The new vorticities $\Omega'_{i,j}$ are next introduced into the stream function equation, which is solved for the new stream function field by the method of successive over-relaxation. Thus, if $\Psi^{(s)}_{i,j}$ denotes the approximate stream function at a point after $s$ iterations, a further approximation $\Psi^{(s+1)}_{i,j}$ is obtained from

$$\Psi^{(s+1)}_{i,j}=(1-\omega)\Psi^{(s)}_{i,j}+\left\{\omega\Big/\left[\frac{2}{(\Delta X)^2}+\frac{1}{(\Delta R)^2}\left(\frac{j}{j+1/2}+\frac{j}{j-1/2}\right)\right]\right\}\times\left\{j\Delta R\Omega'_{i,j}+\frac{1}{(\Delta X)^2}[\Psi^{(s)}_{i+1,j}+\Psi^{(s+1)}_{i-1,j}]+\frac{1}{(\Delta R)^2}\left[\frac{j}{j+1/2}\Psi^{(s)}_{i,j+1}+\frac{j}{j-1/2}\Psi^{(s+1)}_{i,j-1}\right]\right\}. \tag{11}$$

The optimum value of the relaxation parameter $\omega$ can be calculated for a given system of grid points. For the system used in the present study, a value $\omega = 1{\cdot}9$ was used and gave good convergence after thirty-five iterations.†

The new wall vorticities are then calculated from the stream function field in the vicinity of the wall. The defining equation for vorticity (2) reduces to $\Omega = -(1/R)\partial^2\Psi/\partial X^2$ along the top and bottom walls and to $\Omega = -(1/R_b)\partial^2\Psi/\partial R^2$ along the vertical wall. A combination of Taylor series expansions for $\Psi$ near the walls, together with the boundary conditions that $\Psi$ and its normal derivative be zero, yields wall vorticity approximations such as the following, which applies along the bottom

$$\Omega'_{0,j}=-\frac{8\Psi_{1,j}-\Psi_{2,j}}{2(j\Delta R)(\Delta X)^2}. \tag{12}$$

Thus, the new wall vorticities are computed from stream functions which, through (11), were themselves just calculated from the new vorticities at interior grid points.

Finally, new fields of $U$ and $V$ are obtained from three-point central difference approximations to the velocity equations. The fields of $\theta$, $\Omega$, $\Psi$, $U$ and $V$ are thus made current at time level $\tau' = \tau + \Delta\tau$.

The foregoing finite difference approximations conserve energy and vorticity within the grid system. If the equations for temperature, (8) and (10), or vorticity (9) are summed over all interior grid points, no spurious sources or sinks of these quantities are found. The net energy or vorticity transport from the wall mesh points into the enclosure just balances the net increase of energy or vorticity within the mesh sysem. Heat transfer rates to and from the enclosure can thus

† The method of successive over-relaxation is described by Todd (1962, pp. 392–4).

be determined by calculating the transfer from wall mesh points. At steady state, when there is no net increase of energy within the enclosure, the heat transfer into the enclosure balances the heat removed. The foregoing conservation follows partly because of the form used to approximate the convection terms (equations (7)). The importance of care in the choice of this approximation has been noted by Fromm (1964).

### 3.3. *Stability considerations and the time step* $\Delta\tau$

At this point, the size of the time step $\Delta\tau$ for the next time advancement is determined. This is limited by stability considerations which can be given a very simple interpretation. Equations (8), (9) and (10) are rewritten to express $\theta'_{i,j}$ and $\Omega'_{i,j}$ as explicit linear combinations of computed values at time $\tau$;

$$\theta'_{i,j} = a_1\theta_{i+1,j} + a_2\theta_{i-1,j} + a_3\theta_{i,j} + a_4\theta_{i,j+1} + a_5\theta_{i,j-1} \tag{13a}$$

and

$$\Omega'_{i,j} = b_1\Omega_{i+1\,j} + b_2\Omega_{i-1\,j} + b_3\Omega_{i,j} + b_4\Omega_{i,j+1} + b_5\Omega_{i,j-1} + c. \tag{13b}$$

The letters $a$, $b$, and $c$ denote quantities which are constant over a time step.

Stability in the sense of Lax & Richtmyer (1956) follows if the coefficients $a$ and $b$ are all positive; that is, for $k = 1, 2, \ldots, 5$

$$a_k \geqslant 0, \quad b_k \geqslant 0. \tag{14}$$

A rough rule to this effect was stated very simply by Dusinberre (1961, p. 13) for a linear temperature equation; more sophisticated proofs (Lax & Richtmyer 1956 and Barakat & Clark 1966) lead to criteria which are equivalent to (14). Furthermore, Lax & Richtmyer (1956) state that if their stability criterion is met, the initial conditions meet certain requirements (we assume they do), and that the finite difference approximation (13) is consistent with the differential equations (3) and (4), then the solutions of (13) converge to that of (3) and (4) as $\Delta X$, $\Delta R$ and $\Delta\tau$ tend to zero. Thus, stability leads to convergence.

It is not difficult to show that the present finite difference formulation satisfies the stability requirement (14). The coefficients $a_k$, $b_k (k = 1, 2, 4, 5)$ of (13) are always positive, whereas $a_3$ and $b_3$ can be made positive by restricting the size of the time step $\Delta\tau$. In so far as three equations are involved ((8), (9) and (10)) which use special forms similar to (7) to approximate the nonlinear derivatives, several different expressions arise in order to make $a_3, b_3 \geqslant 0$. When $Pr \leqslant 1$ and approximations similar to (7*a*) are used, the temperature equation provides the greatest restriction on $\Delta\tau$. Equation (8) requires that

$$\Delta\tau \leqslant \left[\frac{U_{i+1,j}+U_{i,j}}{2\Delta X} + \left(1+\frac{1}{2j}\right)\frac{V_{i,j+1}+V_{i,j}}{2\Delta R} + \frac{2}{(\Delta X)^2} + \frac{2}{(\Delta R)^2}\right]^{-1}, \tag{15a}$$

whereas equation (10) requires

$$\Delta\tau \leqslant \left[\frac{U_{i+1,0}+U_{i,0}}{2\Delta X} + 2\frac{V_{i,1}}{\Delta R} + \frac{2}{(\Delta X)^2} + \frac{4}{(\Delta R)^2}\right]^{-1}. \tag{15b}$$

Additional forms similar to (15) arise when the alternate approximations (7*b*) are used.

The field of mesh points is scanned in order to determine the largest permissible $\Delta\tau$ which will satisfy the stability requirements. With $\Delta\tau$ thus known,

the field variables $\theta$, $\Omega$, $\Psi$, $U$ and $V$ can be safely advanced across the new time step $\Delta\tau$ by repeating the whole cycle described in §3.2.

The results to be presented in the next section employed a grid spacing of $\Delta X = 0{\cdot}02$ and $\Delta R = 0{\cdot}05$, with a total of 1071 mesh points. This was selected as an optimal spacing to provide good accuracy with a reasonable amount of computer time on the basis of numerical experiments at $Gr = 4 \times 10^6$ and $4 \times 10^7$. This spacing is marginal, however, for the resolution of velocity gradients at higher $Gr$. A finer mesh spacing in the $X$ direction than in the $R$ direction was used so as to provide a better description of the boundary layer along the ceiling. The time step $\Delta\tau$ used was 95 % of that permitted by stability. A single computation cycle took about one-half second on a high speed electronic computer. Computer time was reduced by updating the fields of $\Psi$, $U$ and $V$ less frequently (typically every five cycles) as steady state was approached. A sensitive indication of the approach to steady state was provided by the overall energy balance on the enclosure. When the heat transfer rates into and out of the enclosure agreed to within 1 %, steady conditions prevailed.†

## 4. Results

This investigation covers a range of Grashof number from $Gr = 4 \times 10^4$ to $4 \times 10^{10}$. A Prandtl number typical of air and other gases was assumed; $Pr = 0{\cdot}7$. The geometry of the enclosure was held fixed with an aspect ratio $R_b = 1$ and a relative heat source size $R_c = 0{\cdot}1$.

The flow patterns and temperature fields are illustrated in figures 2–7 with graphs displaying sets of streamlines and isotherms. The location of these streamlines and isotherms was determined by linear interpolation of the computed values at the mesh points. In each of the graphs, the centreline of the cylindrical enclosure is shown on the left. The abscissa is the radial co-ordinate $R$, and the ordinate is the axial co-ordinate $X$. The heat source on the floor is denoted with a thick line between $R = 0$ and $R = 0{\cdot}1$. Additional heat transfer results, velocity profiles, temperature profiles, and trends with $Gr$ are illustrated in figures 4 and 8–11.

### 4.1. *Steady-state streamline and temperature fields*

The variation of the steady-state streamline field with Grashof number is illustrated in figure 2. This figure contains six individual graphs, which respectively pertain to the sequence $Gr = 4 \times 10^4$ to $4 \times 10^9$. In each graph, a dot indicates the location of the maximum value of stream function, $\Psi_{max}$; the numerical value of which is listed in the caption. The streamlines correspond to $\Psi$ values of 0·1 (0·2) 0·9 of $\Psi_{max}$. The solid walls and centreline correspond to $\Psi = 0$. The direction of fluid motion along the streamlines is denoted with small arrowheads.

The flow pattern for $Gr = 4 \times 10^4$ (figure 2(*a*)), reveals a rolling vortex centred at approximately $R = 0{\cdot}5$, $X = 0{\cdot}5$. The maximum value of stream function, $\Psi_{max}$, occurs at the centre of this vortex. As $Gr$ is increased, the vortex centre moves up and to the right. At the same time, the streamlines near the centreline, the ceiling and the right-hand wall move closer together as a result of higher

† This was true for $Gr$ less than $4 \times 10^{10}$.

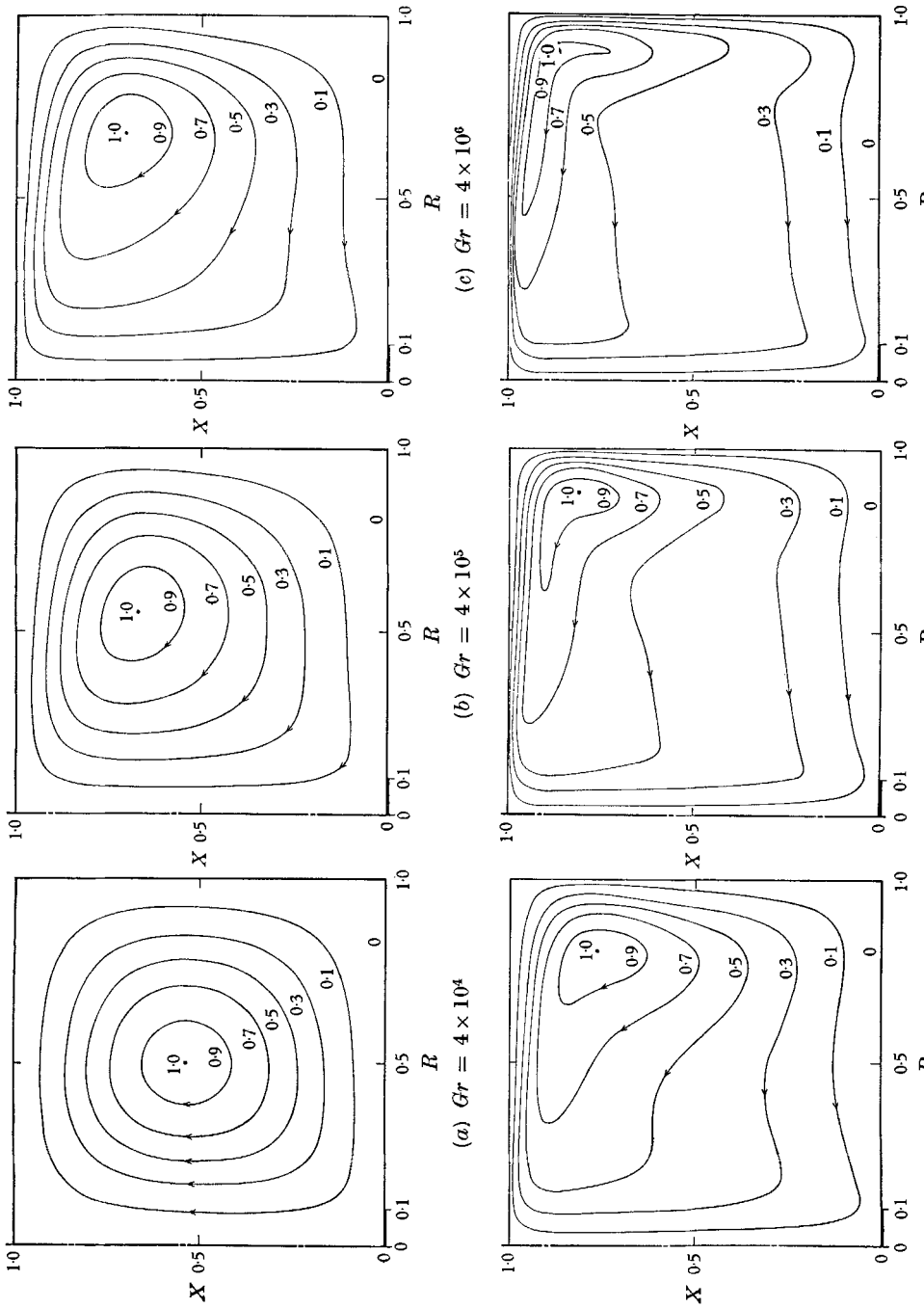


FIGURE 2. Steady-state streamline fields for various Grashof numbers, $Gr$. The streamlines correspond to specified fractions of the maximum value of stream function $\Psi_{max}$, which are as follows: (*a*) $\Psi_{max} = 0{\cdot}719$; (*b*) $\Psi_{max} = 3{\cdot}29$; (*c*) $\Psi_{max} = 8{\cdot}23$; (*d*) $\Psi_{max} = 16{\cdot}7$; (*e*) $\Psi_{max} = 37{\cdot}0$; (*f*) $\Psi_{max} = 103{\cdot}7$.

velocities in these regions. The magnitude of $\Psi_{\max}$ also increases, indicating that more fluid circulation exists.

At $Gr = 4 \times 10^9$ (figure 2(*f*)), the flow is dominated by the rising column of hot gas at $R = 0$. This column entrains surrounding fluid and impacts the ceiling with a resulting stagnation point at $X = 1$, $R = 0$. After impact, a wall jet is formed along the ceiling which flows out radially from the centreline. This layer of warm fluid turns a sharp corner near $X = 1$, $R = 1$ and starts to flow down along the vertical wall. The momentum of the descending fluid carries it well down the wall against the retarding effect of its buoyancy. As the fluid is slowed down, it turns inward and rises to a height determined by its residual buoyancy. The fluid continues to drift slowly inward to be again entrained in the rising column.

The theoretical flow patterns illustrated in figure 2 may be compared with the right-hand halves of experimental photographs for the same geometry presented in figure 4(*a*)–(*e*) of the companion paper, Torrance, Orloff & Rockett (1969). The experimental flows correspond respectively to $Gr = 8 \times 10^5$, $4 \times 10^6$, $4 \times 10^7$, $3 \times 10^8$ and $1 \times 10^{10}$. For $Gr = 4 \times 10^6$ and $4 \times 10^7$ a direct comparison can be made between theory and experiment. The experimental photographs at $Gr = 8 \times 10^5$ and $3 \times 10^8$, on the other hand, must be compared with the nearest theoretical curves, $Gr = 4 \times 10^5$ and $4 \times 10^8$, respectively. For $Gr \leqslant 4 \times 10^7$ the agreement between theory and experiment is seen to be excellent. The experimental results at $Gr = 3 \times 10^8$ closely resemble the theoretical curves at $Gr = 4 \times 10^8$ (figure 2(*e*)). Rather surprisingly, the experimental flow near the ceiling resembles somewhat more closely the theoretical flow at $Gr = 4 \times 10^9$ (figure 2(*f*)). This discrepancy suggests that false viscosity (discussed in connexion with equations (7)) is present near the ceiling in the numerical flow at $Gr = 4 \times 10^8$. In the experiments, turbulence was observed for $Gr \gtrsim 1{\cdot}2 \times 10^9$, and the experimental photograph at $Gr = 1 \times 10^{10}$ illustrates a predominantly turbulent flow. In this photograph, only the flow near the floor is laminar. The theoretical calculation was laminar and completely stable at $Gr = 4 \times 10^9$, presumably due to the introduction of false viscosity. As will be noted in §4.3, the theoretical calculation did develop a periodic vortex shedding when extended to $Gr = 4 \times 10^{10}$.

The variation of the steady-state temperature field with $Gr$ is illustrated in figure 3(*a*)–(*f*). Figure 3(*a*) presents the set of isotherms corresponding to static conduction; whereas 3(*b*)–(*f*) correspond respectively to the sequence $Gr = 4 \times 10^4$ to $4 \times 10^8$. The numerical value of temperature $\theta$ is indicated for each isotherm. The heat source on the floor is at $\theta = 1$, and the remaining solid walls are at $\theta = 0$. The floor temperature distribution is shown in figure 4(*a*). The open circles are the grid approximation of the boundary conditions (6). The dashed line represents the floor temperature distribution appropriate for the lumped mass system.

Isotherms corresponding to static conduction (figure 3(*a*)) were obtained with the present numerical scheme by setting $Gr = 0$ in (9). The effect of convective motion on the temperature field can then be appraised by referring to the static conduction field. Figure 3(*b*)–(*f*) clearly illustrate the effect of the rising column of hot gas on the isotherms above the heat source. Only minor changes of the

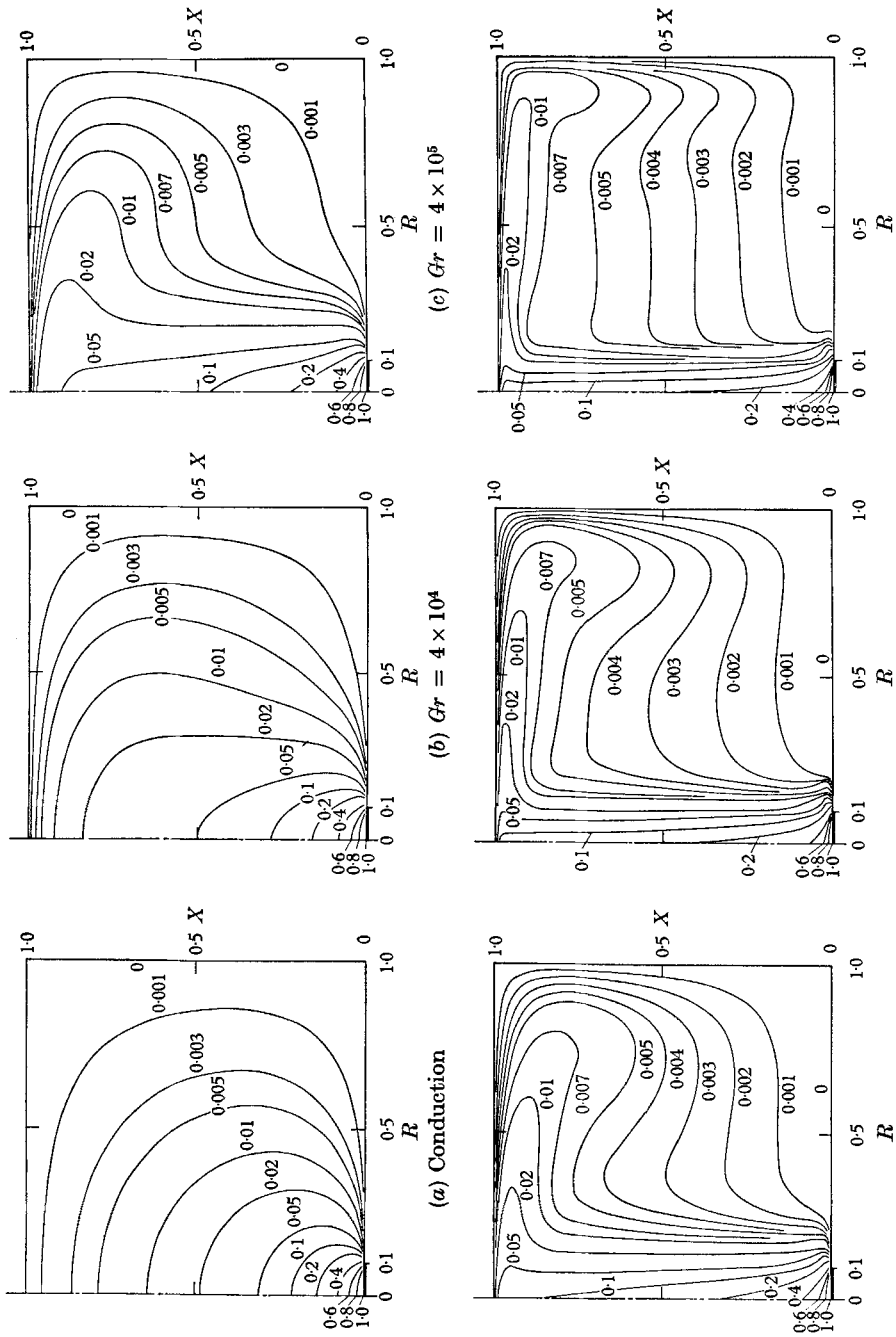


FIGURE 3. Steady-state temperature fields: static conduction and various Grashof numbers, $Gr$. The curve parameter is temperature $\theta$.

isotherms in this region occur for $Gr > 4 \times 10^7$ (figure 3(*e*)) and the column may therefore be considered thermally developed. For $Gr = 4 \times 10^9$ and $4 \times 10^{10}$ the sets of isothermals were found to be similar to those at $4 \times 10^8$ (figure 3(*f*)) and were not reproduced here.

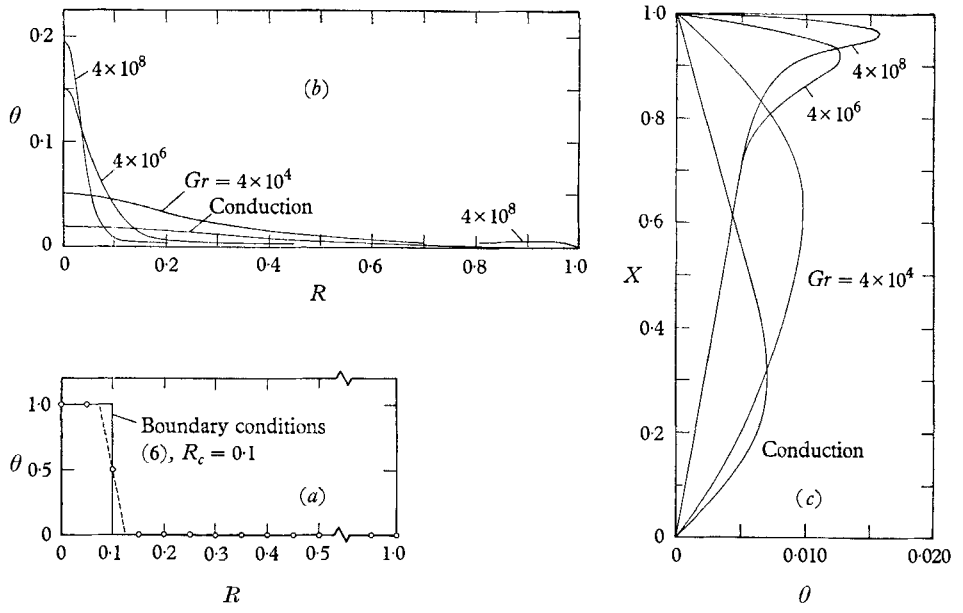


FIGURE 4. Temperature ($\theta$) profiles across the enclosure; (*a*) floor, $X = 0$, --○--, mesh approximation, $51 \times 21$ grid; (*b*) midheight, $X = 0{\cdot}5$; (*c*) midradius, $R = 0{\cdot}5$. Results are shown for static conduction and various Grashof numbers, $Gr$.

Away from the rising column a thermally stratified region develops for $Gr \geqslant 4 \times 10^6$ (figure 3(*d*)–(*f*)). This is made apparent by focusing attention on the isotherms $\theta = 0{\cdot}001$ (0·001) 0·005. These isotherms are roughly equidistant and parallel to the floor for a large portion of the flow region shown in figure 3(*f*). Thus, in this region the temperature increases linearly with increasing height above the floor. This is the region discussed earlier in which the air flows relatively slowly inward to be entrained into the rising hot column.

The linear temperature field associated with the higher Grashof numbers is illustrated in another way in figure 4(*c*), which presents the temperature profile at $R = 0{\cdot}5$ as a function of height $X$. The thermal development of the rising column is apparent in figure 4(*b*), which shows the temperature profile at $X = 0{\cdot}5$ as a function of radius $R$. As $Gr$ increases the hot column becomes more intense and more localized.

### 4.2. *Transient flow development*

The flow and temperature fields discussed in the previous section (figures 2 and 3) were obtained by carrying the theoretical calculation from the initial quiescent condition forward in time until steady state was achieved. The transient flow

fields calculated during this process are illustrated for two values of $Gr$, $4 \times 10^6$ and $4 \times 10^8$, in figures 5 and 6 respectively. The results for $Gr = 4 \times 10^6$ illustrate the general features of the transient flows for low Grashof numbers; whereas the results at $Gr = 4 \times 10^8$ are more typical of the transient flows for the higher Grashof numbers ($\geqslant 4 \times 10^7$). Figures 5 and 6 are each composed of several streamline graphs, arranged in order of increasing time. The captions list the time $\tau$, the maximum value of stream function $\Psi'_{\max}$, and, when less than zero, the minimum value of stream function $\Psi'_{\min}$. Solid streamlines correspond to positive $\Psi'$ values of $\frac{1}{8}$, $\frac{3}{8}$, $\frac{5}{8}$ and $\frac{7}{8}$ of $\Psi'_{\max}$, whereas the dashed streamlines correspond to negative $\Psi'$ values of $\frac{1}{3}$ and $\frac{2}{3}$ of $\Psi'_{\min}$. The dot-dash streamline, together with the solid walls and centreline, have numerical value $\Psi' = 0$. [Figures 5($f$) and 6($l$) illustrate the same steady-state flows as figures 2($c$) and ($e$) respectively, but the streamlines are plotted for a different set of numerical values of $\Psi'$.]

The developing flow for $Gr = 4 \times 10^6$ is shown in figure 5 for times $\tau$ ranging from 0·002 to 0·1. Immediately after the start of heating, a small ring vortex of hot fluid forms near the origin (figure 5($a$)). This vortex rises to the ceiling (5($b$) and ($c$)) and moves radially outward from the centreline (5($d$) and ($e$)). The flow pattern then gradually develops into the steady-state field (figure 5($f$)). A small corner eddy develops during the transient and is shown at its maximum size in figure 5($e$).

A similar sequence of graphs for the developing flow at $Gr = 4 \times 10^8$ is presented in figure 6 for times $\tau$ ranging from 0·0002 to 0·03. Comparison of the transients at $Gr = 4 \times 10^6$ and $4 \times 10^8$ reveals both a similarity and a difference. The similarity is in the motion of the rising ring vortex, the first five graphs at $Gr = 4 \times 10^8$ (6($a$)–($e$)) and at $Gr = 4 \times 10^6$ (5($a$)–($e$)) being almost interchangeable. Indeed, if the time co-ordinate $\tau$ is replaced by $\tau \sqrt{Gr}$ then the time levels are also coincident.† Thus, a similarity exists among the enclosure flows at early times before the viscous drag of the walls becomes important. This follows from the basic equations, (1)–(4), provided diffusion effects are negligible (Scorer 1957). Flows at different $Gr$ are found to be similar if $\Psi'$, $\Omega$, $U$, $V$ and $\tau$ are replaced by $\Psi'/\sqrt{Gr}$, $\Omega/\sqrt{Gr}$, $U/\sqrt{Gr}$, $V/\sqrt{Gr}$ and $\tau \sqrt{Gr}$.

A striking difference between the flows at $Gr = 4 \times 10^6$ and $4 \times 10^8$ is also apparent. The eddy in the lower right corner at $Gr = 4 \times 10^8$ (figure 6($e$)) does not immediately diminish in size as it did at $Gr = 4 \times 10^6$ (figure 5($e$)). Instead the eddy grows in size (figures 6($f$)–($h$)) and then washes away into the main flow (6($i$) and ($j$)). Its effect on the flow is evident for a long time (6($k$)) before steady conditions are achieved (6($l$)). This corner eddy originates when fluid heated by the hot spot slides over cold fluid in the corner. The corner eddy heats up slowly and eventually floats up into the inward moving stream. In general, the size of this corner eddy increases with increasing $Gr$.

Note that the transient streamlines shown in figures 5 and 6 are represented in the Eulerian point of view. The alternate Lagrangian point of view follows the path of individual fluid elements. With such a description, the initial ring vortex would appear as a rising mushroom cloud.

† For comparison purposes, simply multiply the $\tau$ values of figure 6 by ten.

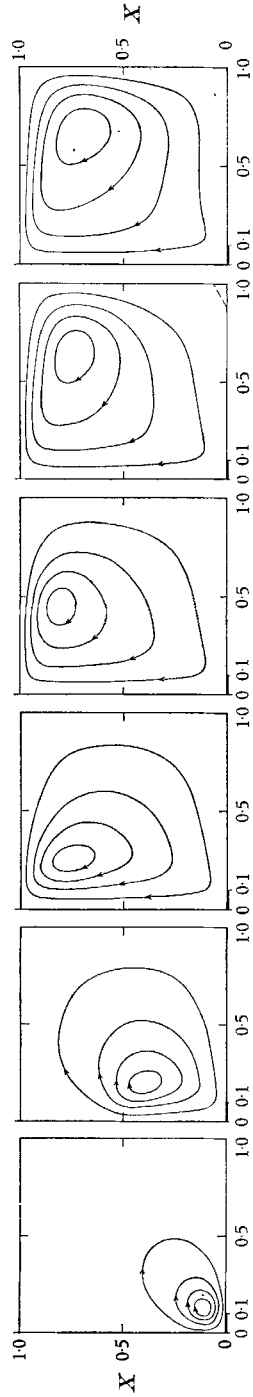


FIGURE 5. Transient streamline fields for $Gr = 4 \times 10^6$ at various times $\tau$. The streamlines correspond to $\Psi'$ values of $\frac{1}{8}$, $\frac{3}{8}$, $\frac{5}{8}$ and $\frac{7}{8}$ of $\Psi'_{max}$. The values of $\Psi'_{max}$ are: (*a*) $\Psi'_{max} = 0{\cdot}80$; (*b*) $\Psi'_{max} = 3{\cdot}62$; (*c*) $\Psi'_{max} = 6{\cdot}46$; (*d*) $\Psi'_{max} = 7{\cdot}97$; (*e*) $\Psi'_{max} = 8{\cdot}24$, $\Psi'_{min} = -0{\cdot}00063$; (*f*) $\Psi'_{max} = 8{\cdot}23$.

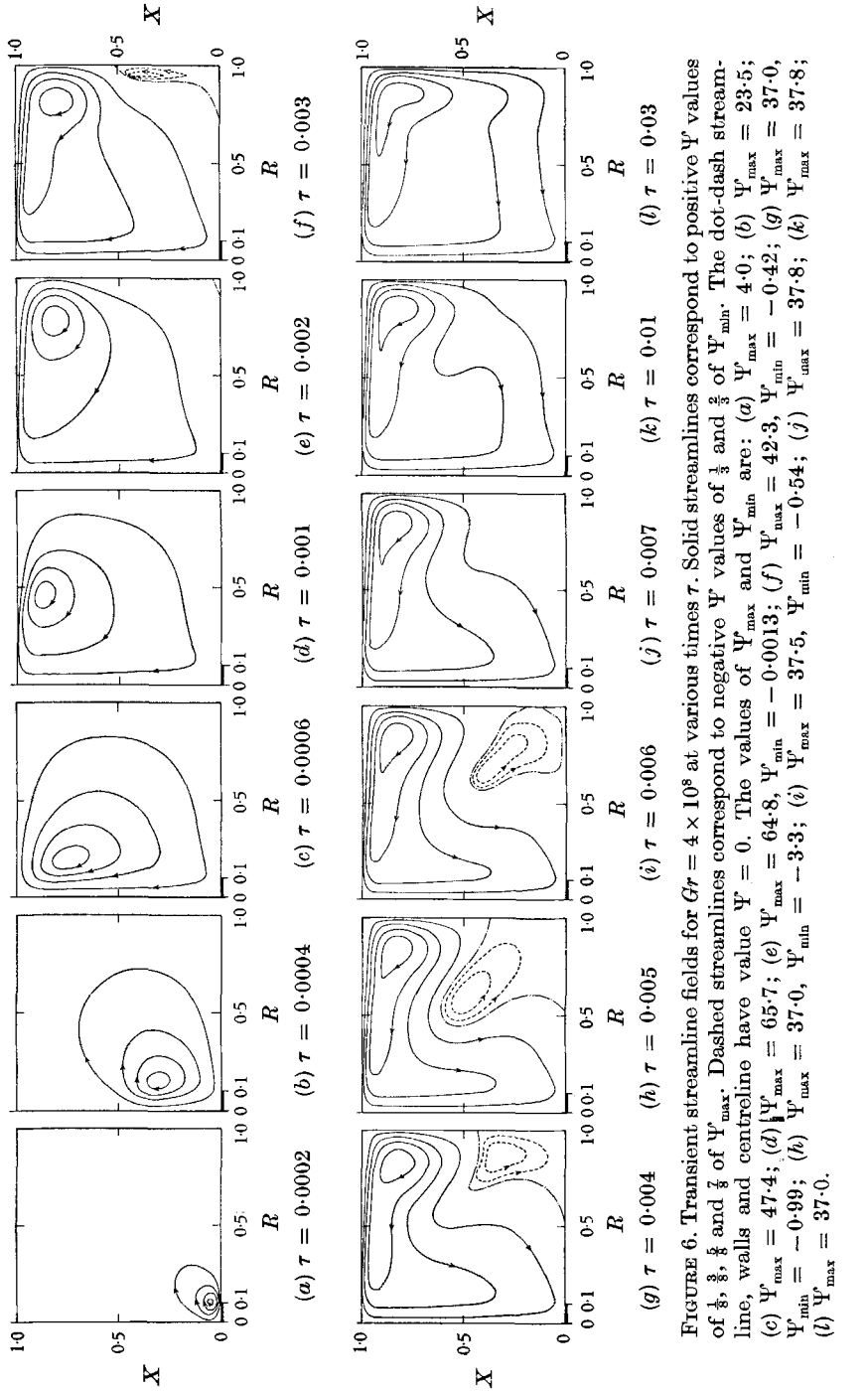


FIGURE 6. Transient streamline fields for $Gr = 4 \times 10^8$ at various times $\tau$. Solid streamlines correspond to positive $\Psi$ values of $\frac{1}{8}$, $\frac{3}{8}$, $\frac{5}{8}$ and $\frac{7}{8}$ of $\Psi_{max}$. Dashed streamlines correspond to negative $\Psi$ values of $\frac{1}{3}$ and $\frac{2}{3}$ of $\Psi_{min}$. The dot-dash streamline, walls and centreline have value $\Psi = 0$. The values of $\Psi_{max}$ and $\Psi_{min}$ are: (*a*) $\Psi_{max} = 4{\cdot}0$; (*b*) $\Psi_{max} = 23{\cdot}5$; (*c*) $\Psi_{max} = 47{\cdot}4$; (*d*) $\Psi_{max} = 65{\cdot}7$; (*e*) $\Psi_{max} = 64{\cdot}8$, $\Psi_{min} = -0{\cdot}0013$; (*f*) $\Psi_{max} = 42{\cdot}3$, $\Psi_{min} = -0{\cdot}42$; (*g*) $\Psi_{max} = 37{\cdot}0$, $\Psi_{min} = -0{\cdot}99$; (*h*) $\Psi_{max} = 37{\cdot}0$, $\Psi_{min} = -3{\cdot}3$; (*i*) $\Psi_{max} = 37{\cdot}5$, $\Psi_{min} = -0{\cdot}54$; (*j*) $\Psi_{max} = 37{\cdot}8$; (*k*) $\Psi_{max} = 37{\cdot}8$; (*l*) $\Psi_{max} = 37{\cdot}0$.

### 4.3. *Vortex shedding at* $Gr = 4 \times 10^{10}$

The preceding sections presented results for $Gr$ in the range $4 \times 10^4$ to $4 \times 10^9$. Comparison with experiment (Torrance *et al.* 1969) supports the validity of a laminar flow calculation for $Gr \lesssim 1{\cdot}2 \times 10^9$. Just above $Gr \approx 1{\cdot}2 \times 10^9$, experiment indicates the onset of turbulence. As discussed in §3·2 of the aforementioned paper, the first appearance of turbulence was in the form of small eddies which appeared semi-periodically at the edge of the rising column as it impacted the ceiling. These eddies rolled out along the ceiling, turned downward near the outer wall, and eventually diffused into the general flow of air returning to the rising column. Except for these eddies, the flow was laminar. The numerical calculations are two-dimensional, and cannot describe three-dimensional turbulent motion. In addition, a false numerical viscosity is introduced at high $Gr$ (as evidenced by the completely stable theoretical flow at $Gr = 4 \times 10^9$ in figure 2($f$)). Nevertheless, for the purpose of exploring the onset of laminar instability, the present numerical method was applied to still higher $Gr$.

Accordingly, a run at $Gr = 4 \times 10^{10}$ starting from the initial quiescent conditions was undertaken. The initial transient flow exhibited the same gross features as already noted for $Gr = 4 \times 10^8$ in figure 6. After the corner eddy had washed into the main flow, the calculation revealed a new phenomenon. Namely, a periodic shedding of ring vortices within the fluid. These vortices originated near the corner formed by the ceiling and outer wall of the cylindrical enclosure. After shedding, these vortices drifted along with the general flow until diffused. Extension of the calculation revealed that a time-independent fully developed flow did not exist. Instead, the fully developed flow contained this periodic vortex shedding. The similarity between this vortex shedding and the experimentally observed onset of turbulence described above is striking.

The fully developed theoretical flow for $Gr = 4 \times 10^{10}$ can be studied with the aid of figure 7, which illustrates the streamline field at a particulr instant of time ($\tau = 0{\cdot}0081$). The streamlines correspond to specified fractions of $\Psi'_{\max}$, the value of which is listed in the caption. Within the flow field four small vortices appear which are centred at $A$, $B$, $C$ and $D$. The locations of these vortices were determined by searching the stream function field for local maxima. In all the vortices, the rotational sense is clockwise.

The four vortices were generated in succession at equally spaced intervals of time corresponding to the vortex shedding period. For the conditions of the figure, the period was 0·00165 dimensionless time units. The vortex $A$ is about to be shed from the general flow of fluid along the 0·9 streamline. The vortices $B$, $C$ and $D$ were similarly shed 0·00165, 0·00330 and 0·00495 time units earlier, respectively. Vortex $A$ will move successively to positions $B$, $C$, and $D$ after intervals of 0·00165 time units. In the course of movement along its path, the vortex is diffused and decreases in strength. At position $D$, the vortex is sufficiently weak so as to be barely discernible. Indeed, a short time later it disappears into the general fluid motion.

The vortex shedding which appeared at $Gr = 4 \times 10^{10}$ was adequately resolved with a grid spacing of $\Delta X = 0{\cdot}02$ and $\Delta R = 0{\cdot}05$. It was our suspicion that

flows at higher $Gr$ would require a somewhat finer grid to maintain adequate spatial resolution. The corresponding increase in computer time did not seem justifiable; therefore, calculations at $Gr$ greater than $4 \times 10^{10}$ were not considered.

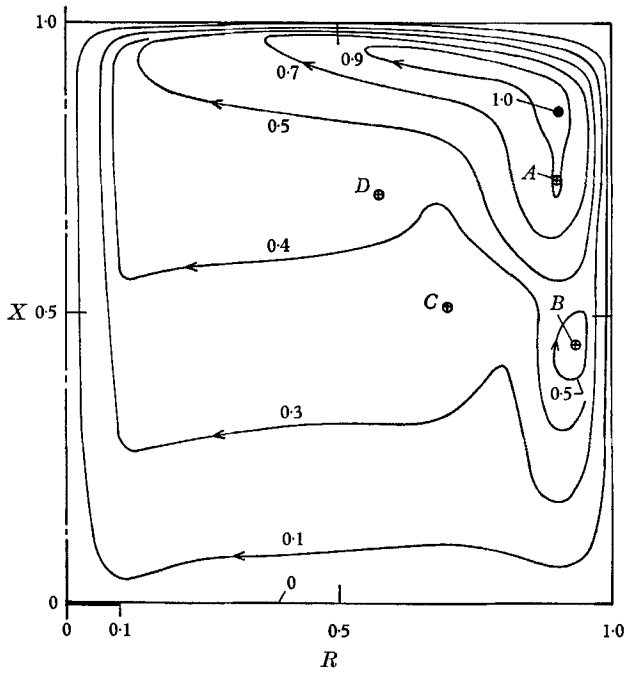


FIGURE 7. Streamline field for $Gr = 4 \times 10^{10}$ at time $\tau = 0{\cdot}0081$. The streamlines correspond to specified fractions of the maximum value of stream function, $\Psi'_{max} = 366$. Four small vortices appear within the flow at $A$, $B$, $C$ and $D$.

### 4.4. *Heat transfer rates, velocity profiles and trends with Gr*

The heat transfer results are conveniently discussed in terms of the rate of heat addition ($\dot{Q}_{in}$) or heat removal ($\dot{Q}_{out}$) from the enclosure. These are total quantities, obtained by integration over the areas of the heat source and cold walls, respectively. The integration is performed by computing the heat transfer from wall mesh points to adjacent mesh points, as discussed in the paragraph at the end of §3.2. The heat transfer rates discussed in this section apply for the ramp change in temperature at the edge of the heat source shown by the dashed line in figure 4(*a*). This ramp is a close approximation of the floor temperature profile in the physical experiments of the companion paper. Both numerically and experimentally, the step change in temperature specified by the boundary conditions (6) is difficult to achieve. The rates of heat transfer, while being finite for a ramp, would be infinite for a step.

The heat transfer rates $\dot{Q}_{in}$ or $\dot{Q}_{out}$ can be used to define an average heat transfer coefficient $\bar{h}$ in terms of the heating or cooling area $A$ and the imposed temperature difference $\Delta T = T_h - T_0$.

$$\dot{Q} = \int_A d\dot{Q} = \bar{h} A \Delta T. \tag{16}$$

This equation defines the rates of heat addition ($\dot{Q}_{\text{in}}$) or heat removal ($\dot{Q}_{\text{out}}$) when the area $A$ is the heating or cooling surface, respectively. The average Nusselt number can be expressed in terms of $\dot{Q}$ as

$$\overline{Nu}_l = \frac{\bar{h}l}{\lambda} = \frac{1}{\mathscr{A}}\frac{\dot{Q}}{\lambda l \Delta T}, \tag{17}$$

where $l$ is a characteristic length, $\lambda$ the thermal conductivity of the fluid, and $\mathscr{A}$ the dimensionless heating or cooling area, $\mathscr{A} = A/l^2$.

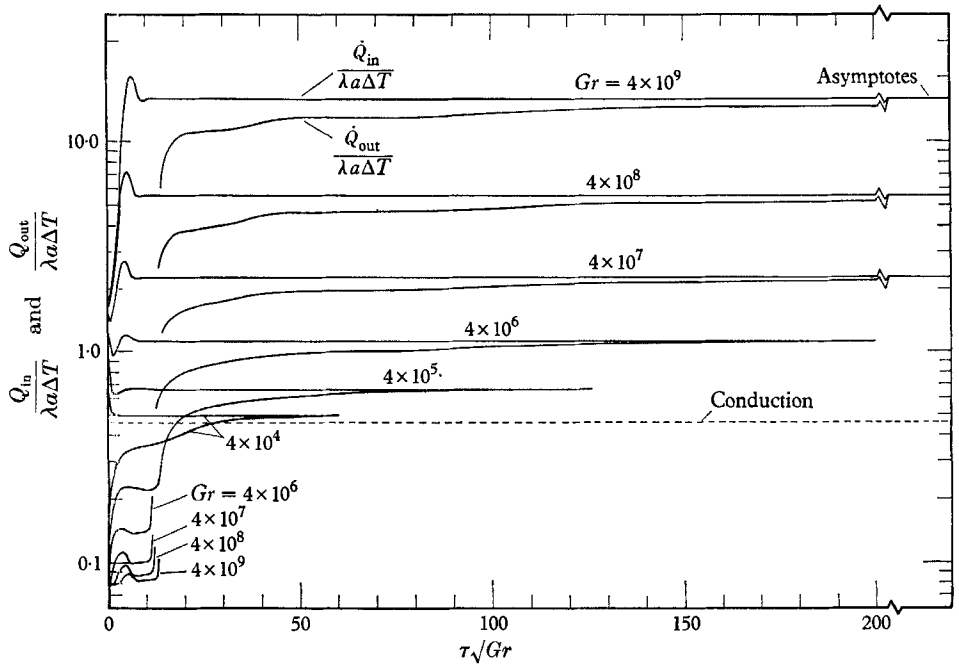


FIGURE 8. Heat flow into ($\dot{Q}_{\text{in}}/\lambda a \Delta T$) and out of ($\dot{Q}_{\text{out}}/\lambda a \Delta T$) the enclosure for various Grashof numbers ($Gr$) as a function of scaled time $\tau\sqrt{Gr}$. The temperature difference $\Delta T = (T_h - T_0)$.

Curves illustrating the heat transfer rates into and out of the enclosure as a function of time are presented in figure 8. The ordinate is the dimensionless ratio $\dot{Q}/\lambda a \Delta T$, which follows from (17) when the characteristic length is the enclosure height $a$. The abscissa is $\tau\sqrt{Gr}$, a combination which scales the transients at early times as discussed in §4.2. The curve parameter is $Gr$, which ranges from $4\times10^4$ to $4\times10^9$. For each $Gr$ two curves are shown, the upper and lower curves respectively corresponding to the rates of heat transfer into ($\dot{Q}_{\text{in}}/\lambda a \Delta T$) and out of ($\dot{Q}_{\text{out}}/\lambda \alpha \Delta T$) the enclosure. The dashed line corresponds to the steady-state static conduction value.

A comparison of the upper curves at each $Gr$ reveals that the heat transfer rates increase monotonically from the conduction value with increasing $Gr$. Furthermore, there is a similarity in the shape of the curves at higher $Gr$. A maximum in these curves appears at about $\tau\sqrt{Gr} = 6$, and is followed by a slight undershoot before essentially approaching the steady-state value by $\tau\sqrt{Gr} = 12$.

This overshoot and undershoot is caused by the rotation of the ring vortex shown in figures 5(*a*) and 6(*a*) as it brings in first cold fluid and then warm fluid to the heat source. The steady-state heat transfer rate is achieved before the rising ring vortex reaches the ceiling, as shown in figures 5(*c*) and 6(*c*), which correspond to $\tau\sqrt{Gr} = 12$.

A comparison of the lower curves at each $Gr$ in figure 8 also reveals some similarities. For $\tau\sqrt{Gr} < 12$, the rate of heat removal from the enclosure is low. This rate decreases with increasing $Gr$, as it becomes more difficult for heat to be conducted radially from the heat source to the nearby cold floor counter to the incoming flow. At about $\tau\sqrt{Gr} = 12$, the rate of heat removal increases sharply as the hot, rising vortex hits the ceiling (figures 5(*c*) and 6(*c*), for example). As the hot fluid spreads radially outward along the ceiling, the rate of heat removal continues to rise. For $\tau\sqrt{Gr} > 30$, the cooling abilities of the vertical wall and floor are also brought into play, and the lower curve gradually approaches the upper curve. At the higher $Gr$, the heat transfer curves are generally similar for $\tau\sqrt{Gr}$ less than about 40. For $\tau\sqrt{Gr}$ greater than this value, the curves describing the rates of heat removal are not similar. These differences are associated with the development and movement of the corner eddy discussed in §4.2.

The above discussion points out that the rate of heat addition to the enclosure achieves a steady value long before the flow itself is at steady state. In particular, the steady rate exists before the rising vortex reaches the ceiling. Hence, we conclude that the rate of heat addition ($\dot{Q}_{\text{in}}/\lambda a \Delta T$) is probably independent of enclosure shape. The numerical calculations thus provide the heat transfer rates for a related problem: the heated disk of diameter $d\,(=2c)$ in an infinite horizontal flat plate with a floor temperature profile as shown by the dashed line in figure 4(*a*). Using $d$ as the characteristic length, we introduce a mean Nusselt number $\overline{N}u_d$ from equation (17) and a Grashof number $Gr_d = g\beta\Delta T d^3/\nu^2$.

Theoretical and experimental results for steady-state heat transfer are shown in figure 9 with $\log \overline{N}u_d$ as ordinate and $\log Gr_d$ as abscissa. The filled circles are numerical results from the present study, whereas the squares are experimental results from table 1 of the companion paper, Torrance *et al.* (1969). The agreement between experiment and theory is encouraging. For comparison, a curve is included which illustrates the heat transfer from spheres suspended in a gas. This is based on the experiments of Kyte, Madden & Piret (1953), for the case when rarefied gas effects are absent. The two curves are generally similar. Both curves approach the static conduction value as $Gr_d \to 0$. For large $Gr_d$, $\overline{N}u_d$ is proportional to $Gr_d^{\frac{1}{4}}$ for spheres and to $Gr_d^{\frac{1}{2}}$ for the heated disk. The difference in exponents is a result of the two vastly different flow situations.

At several times in the foregoing, we have discussed the scaling of the transient flows. Early in the transient, the time co-ordinate was scaled with $\tau\sqrt{Gr}$, a result which follows from the basic equations when viscosity is neglected. For $\tau\sqrt{Gr} > 40$ in the transient, this scaling no longer applied because viscous drag on the walls had developed. Nevertheless, we can focus our attention on the end result of the transients, i.e. the fully developed flows, and inquire if they exhibit any scaling with $Gr$. Presumably, as $Gr$ is increased, viscous effects become less important than inertia effects, and the velocities, stream function and vorticity ought to

scale with $U/\sqrt{Gr}$, $V/\sqrt{Gr}$, $\Psi/\sqrt{Gr}$ and $\Omega/\sqrt{Gr}$, as in the early transient. For low $Gr$, when viscous effects are more important than inertia effects, the foregoing scaling would be $U/Gr$, $V/Gr$, $\Psi/Gr$ and $\Omega/Gr$.

Figure 10 was prepared to display the variation of the maximum velocity and maximum stream function with $Gr$. The maximum vector velocity occurred along the centreline and is identical with the maximum $U$ component. The

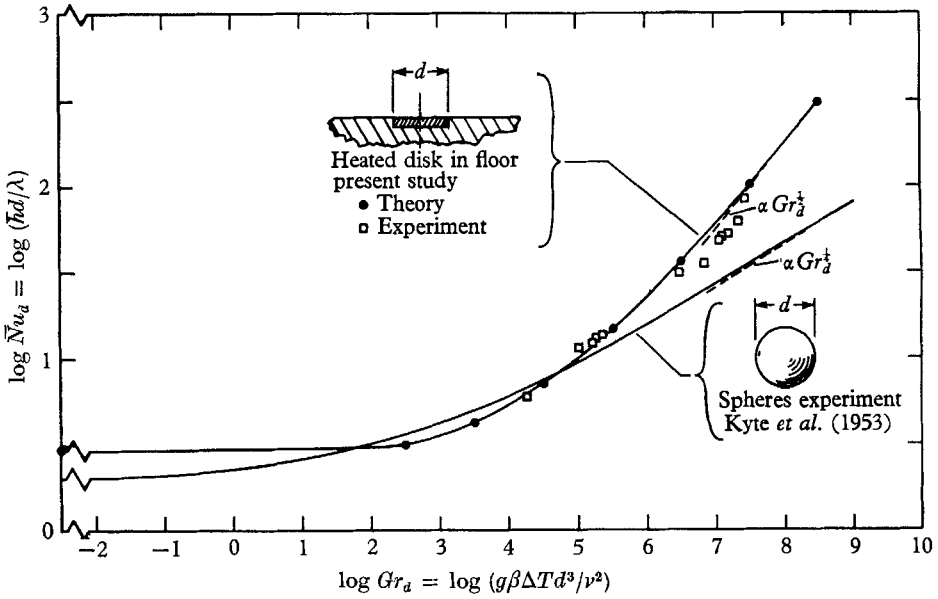


FIGURE 9. Mean Nusselt number *versus* Grashof number. Characteristic length $d$, temperature difference $\Delta T = (T_h - T_0)$.

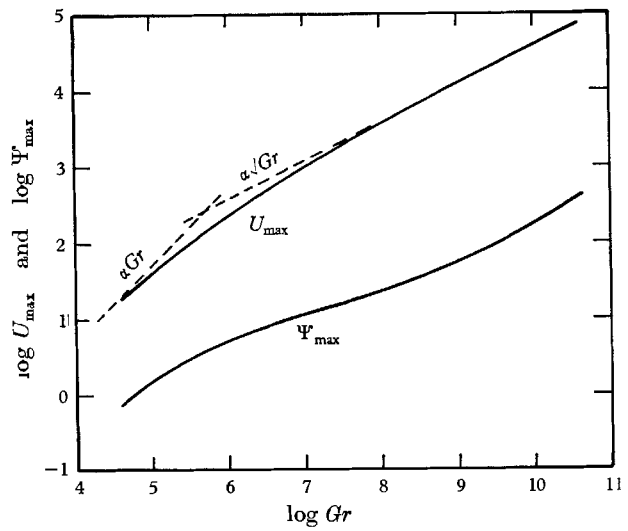


FIGURE 10. Maximum velocity $U_{max}$ and maximum stream function $\Psi_{max}$ *versus* Grashof number.

ordinate is $\log U_{\max}$ or $\log \Psi_{\max}$ and the abscissa is $\log Gr$. Comparison of the slopes of the curves for $U_{\max}$ and $\Psi_{\max}$ with the dashed lines, which are proportional to $Gr$ and $\sqrt{Gr}$, suggests a proportionality to $Gr$ for low $Gr$ and to $\sqrt{Gr}$ for large $Gr$.

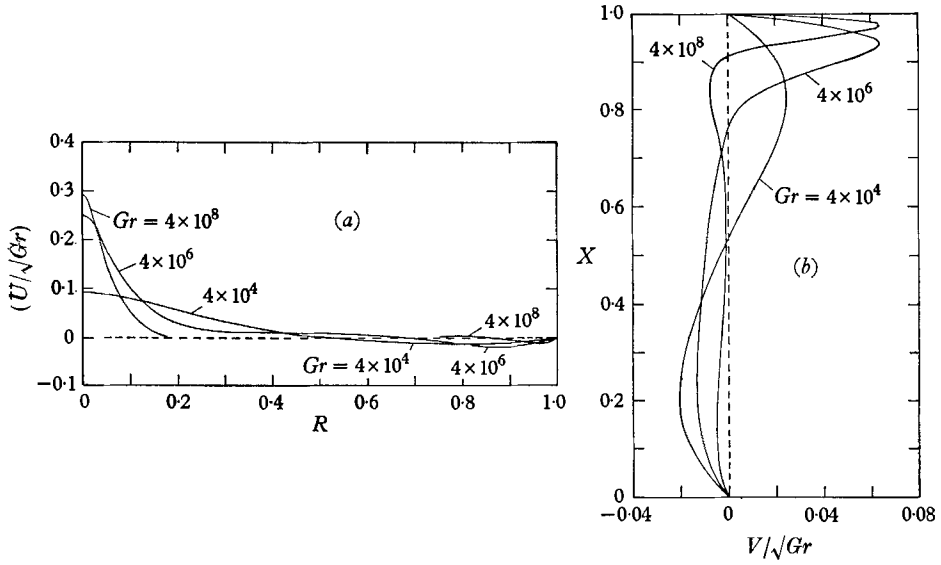


FIGURE 11. Scaled velocity profiles across the enclosure for various Grashof numbers. (*a*) $U/\sqrt{Gr}$ at the midheight, $X = 0{\cdot}5$. (*b*) $V/\sqrt{Gr}$ at the mid-radius, $R = 0{\cdot}5$.

Additional evidence for the scaling of $U$ and $V$ with $U/\sqrt{Gr}$ and $V/\sqrt{Gr}$ is provided in figure 11. Figure 11(*a*) presents the scaled vertical velocity profile $U/\sqrt{Gr}$ at the mid-height as a function of radius $R$. The $U/\sqrt{Gr}$ profiles for $Gr > 4\times10^8$ are indistinguishable near the centreline from results for $Gr = 4\times10^8$. Figure 11 (*b*) shows the scaled radial velocity $V/\sqrt{Gr}$ at the midradius as a function of height $X$.

The authors would like to thank Professor Howard W. Emmons of Harvard University for many helpful discussions during the course of this work. This paper is a contribution of the National Bureau of Standards and is not subject to copyright.

## REFERENCES

BARAKAT, H. Z. & CLARK, J. A. 1966 Analytical and experimental study of the transient laminar natural convection flows in partially filled liquid containers. Proceedings of the *Third International Heat Transfer Conference* (August 7–12, 1966, Chicago, Illinois), prepared by the American Institute of Chemical Engineers, vol. II, 152.

DUSINBERRE, G. M. 1961 *Heat Transfer Calculations by Finite Differences*. Scranton: International Textbook Company.

FROMM, J. 1964 The time dependent flow of an incompressible viscous fluid. *Methods in Computational Physics*, vol. 3. New York: Academic.

KYTE, J. R., MADDEN, A. J. & PIRET, E. L. 1953 Natural-convection heat transfer at reduced pressure. *Chem. Eng. Prog.* **49**, 653.

LAX, P. D. & RICHTMYER, R. D. 1956 Survey of the stability of linear finite difference equations. *Comm. Pure Appl. Math.* **9**, 267.

MILNE-THOMSON, L. M. 1960 *Theoretical Hydrodynamics*, fourth edition. New York: Macmillan.

SCORER, R. S. 1957 Experiments on convection of isolated masses of buoyant fluid. *J. Fluid Mech.* **2**, 583.

TODD, J. 1962 *Survey of Numerical Analysis*. New York: McGraw–Hill.

TORRANCE, K. E. 1968 Comparison of finite-difference computations of natural convection. *J. Research of the National Bureau of Standards—B. Mathematical Sciences*, **72B**, 281.

TORRANCE, K. E., ORLOFF, L. & ROCKETT, J. A. 1969 Experiments on natural convection in enclosures with localized heating from below. *J. Fluid Mech.* **36**, 21.

WILKES, J. O. & CHURCHILL, S. W. 1966 The finite-difference computation of natural convection in a rectangular enclosure. *Am. Inst. Chem. Eng. J.* **12**, 161.